

Self-Assembly Behavior of an Oligothiophene-Based Conjugated Liquid Crystal and Its Implication for Ionic Conductivity Characteristics

Ziwei Liu, Ban Xuan Dong, Mayank Misra, Yangyang Sun, Joseph Strzalka, Shrayesh N. Patel, Fernando A. Escobedo,* Paul F. Nealey,* and Christopher K. Ober*

In this work, a joint experimental and computational study on the synthesis, self-assembly, and ionic conduction characteristics of a new conjugated liquid crystal quaterthiophene/poly(ethylene oxide) (PEO4) consisting of terminal tetraethyleneglycol monomethyl ether groups on both ends of a quaterthiophene core is performed. In agreement with molecular dynamic simulations, temperature-dependent grazing-incidence wide angle X-ray scattering and X-ray diffraction indicate that the molecule spontaneously forms a smectic phase at ambient temperature as characterized both in bulk and thin film configurations. Significantly, this smectic phase is maintained upon blending with bis(trifluoro-methanesulfonyl)imide as ion source at a concentration ratio up to $r = [\text{Li}^+]/[\text{EO}] = 0.05$. Nanosegregation between oligothiophene and PEO moieties and π - π stacking of thiophene rings lead to the formation of efficient 2D pathways for ion transport, resulting in thin-film in-plane ionic conductivity as high as $5.2 \times 10^{-4} \text{ S cm}^{-1}$ at 70°C and $r = 0.05$ as measured by electrochemical impedance spectroscopy. Upon heating the samples above a transition temperature around 95°C , an isotropic phase forms associated with a pronounced drop in ionic conductivity. Upon cooling, partial and local reordering of the conducting smectic domains leads to an ionic conductivity decrease compared to the as-cast state.

the crystalline phase, but they are easier to align homogeneously and spontaneously over large areas.^[3] Ordered self-assembled molecules can induce enhanced properties and functions,^[4] thus enabling specific applications in a wide variety of advanced technologies.^[5,6] The idea of using LCs for ion^[7–10] and electron^[5,6,11,12] transport has attracted much attention in recent decades. The spontaneous phase segregation between immiscible parts^[5,6,13–15] enables the use of LCs as anisotropic ion conductors, making them promising candidates for energy devices. Moreover, their properties of fast assembly and easy processability^[16] excel those of traditional electrolytes. By tuning the molecular shape and intermolecular interactions, mesogenic molecules can self-assemble into a range of LC nanostructures such as columnar, smectic, or bicontinuous cubic phases, providing 1D,^[17–19] 2D,^[20–24] and 3D^[7,25–28] ion transport pathways. These molecules have been proposed for potential application as efficient and stable electrolytes for batteries and dye-sensitized

solar cells.^[10,29–33] 1D and 2D channels formed by discotic and rod-like LCs, respectively, are mostly studied.


In general, ion-conducting LCs consist of polar or ionic groups such as cyclic carbonates,^[10,32–34] poly(ethylene oxide)s (PEOs),^[20,21,35,36] or cationic and anionic moieties attached to rod-like or wedge-shaped moieties to achieve columnar

1. Introduction

Liquid crystals (LCs) are thermodynamically stable phases with an intermediate degree of order between the isotropic melt (amorphous) and the crystal (perfectly regular).^[1–3] In LC phases, the molecules exhibit lower order and density than in

Z. Liu, Prof. C. K. Ober
Department of Materials Science and Engineering
Cornell University
Ithaca, NY 14853, USA
E-mail: cko3@cornell.edu

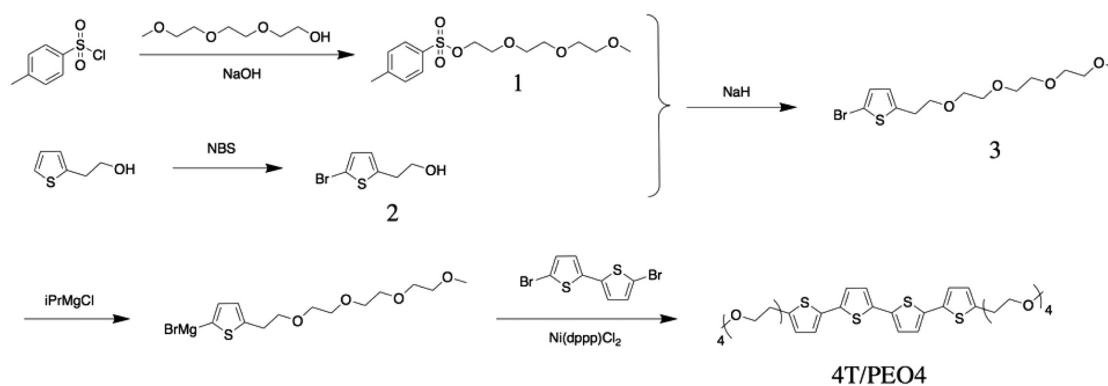
Dr. B. X. Dong, Prof. S. N. Patel, Prof. P. F. Nealey
Institute for Molecular Engineering
University of Chicago
Chicago, IL 60637, USA
E-mail: nealey@uchicago.edu

 The ORCID identification number(s) for the author(s) of this article can be found under <https://doi.org/10.1002/adfm.201805220>.

Dr. M. Misra, Y. Sun, Prof. F. A. Escobedo
School of Chemical and Biomolecular Engineering
Cornell University
Ithaca, NY 14853, USA
E-mail: fe13@cornell.edu

Dr. J. Strzalka
X-Ray Science Division
Argonne National Laboratory
Argonne, IL 60439, USA
Prof. S. N. Patel, Prof. P. F. Nealey
Materials Science Division
Argonne National Laboratory
Lemont, IL 60439, USA

DOI: 10.1002/adfm.201805220



Scheme 1. Synthetic procedure of 4T/PEO4.

and smectic structures.^[37] The 2D arrangement of smectics is believed to be more tolerant with regard to defects than 1D ordered columns and provides more directions for ion transport therefore results in an improved performance.^[3] Despite large amount of recent work focusing on ionic conduction achieved by small ionic or cyclic carbonate moieties, PEO remains a popular component for ion-transport LCs. Extensive studies have shown that PEO possesses excellent solvating capability for a wide range of lithium salts, and inherently high ionic conductivity and facile processability.^[38] In these molecules, PEO moieties are usually attached to mesogenic fragments so that the coexistence of ion-conducting and nonconducting phases induces better phase segregation and ions are transported through segmental motion of PEO fragments.

Phase segregation and self-assembly provide additional functionality and stability to LC materials. Generally, segregation is favored in molecules with well-defined intramolecular contrast, such as distinct rigid and flexible segments. Apart from specific intermolecular interactions such as hydrogen bonding and ionic interactions that play key roles in the formation of complex structures, π - π stacking interaction is also considered one of the very important noncovalent interactions as driving force for molecules to achieve hierarchical self-assembly.^[39,40] Abundant evidence from the columnar stacking of discotic LC molecules suggests that self-assembly through strong π - π stacking could be an effective approach to 1D nanostructures for planar, rigid organic molecules,^[6,41] and it could also be effective to obtain 2D nanostructures with calamitic molecules. π - π stacking has in fact been observed in many oligothiophenes and their derivatives.^[42–48] Experimental measurements indicate that π - π interaction plays an important role in the control of the solid-state and self-assembled structures of thiophene oligomers and polymers.^[49,50]

To this end, we report the synthesis and characterization of a coil-rod-coil π -conjugated LC compound (quaterthiophene (4T)/PEO4) consisting of oligothiophene and ethylene oxide moieties. The rigid rod mesogen consists of four thiophene rings whereas the flexible tetra(ethylene oxide) segments on both ends of the mesogen core function as ion transport domains. Oligothiophene moieties, commonly used in flexible electronics, were chosen to endow electron transport properties to the compound for a promising mixed ionic/electronic conducting material. Using both grazing incidence wide-angle X-ray scattering (GIWAXS) and molecular dynamics (MD) simulation, we show

that the compound exhibits ordered smectic phases in the absence and presence of lithium bis(trifluoromethanesulfonyl) imide (LiTFSI) at concentration $r = [\text{Li}^+]/[\text{EO}]$ up to 0.05. Temperature-dependent GIWAXS and MD simulations indicated that π - π interaction among mesogens also plays a key role in controlling LC self-assembly. Further, ionic conductivity is measured by electrochemical impedance spectroscopy (EIS) for different doping ratios ranging from 25 to 130 °C. Our results provide important new insights into self-assembly behavior of this class of π -conjugated LCs and their morphology-ion transport relationship.

2. Results and Discussion

2.1. Synthesis of Liquid Crystalline Material 4T/PEO4

A quaterthiophene-based π -conjugated LC compound designated 4T/PEO4, has been designed and synthesized as shown in **Scheme 1**. In this molecule, the terminal PEO4 segments are directly attached to both ends of a 4T core without any linker, in order to maximize the volume ratio and ion transport function of PEO moieties. The synthesis of compound 4T/PEO4 was accomplished via twofold Kumada cross-coupling of 5,5'-dibromo-2,2'-bithiophene with three equivalents of the corresponding brominated thiophene-PEO4 precursors in the presence of Ni(dppp)Cl₂ as catalyst. The compound is a viscous dark red solid at room temperature and was characterized by ¹H and ¹³C nuclear magnetic resonance (NMR) spectroscopy (see the Supporting Information).

2.2. Thermal and Structural Properties of Bulk 4T/PEO4-LiTFSI Complexes

The thermal properties of the compound 4T/PEO4 were analyzed by differential scanning calorimetry (DSC). Optical textures of the substances exhibiting LC phases were obtained by polarized optical microscopy (POM). Here, we investigate the structure of 4T/PEO4 blended with LiTFSI which has good thermal stability, high ion dissociation rate, and high ionic conductivity.^[51] Specifically, we choose to study 4T/PEO4-LiTFSI complexes with three different blending

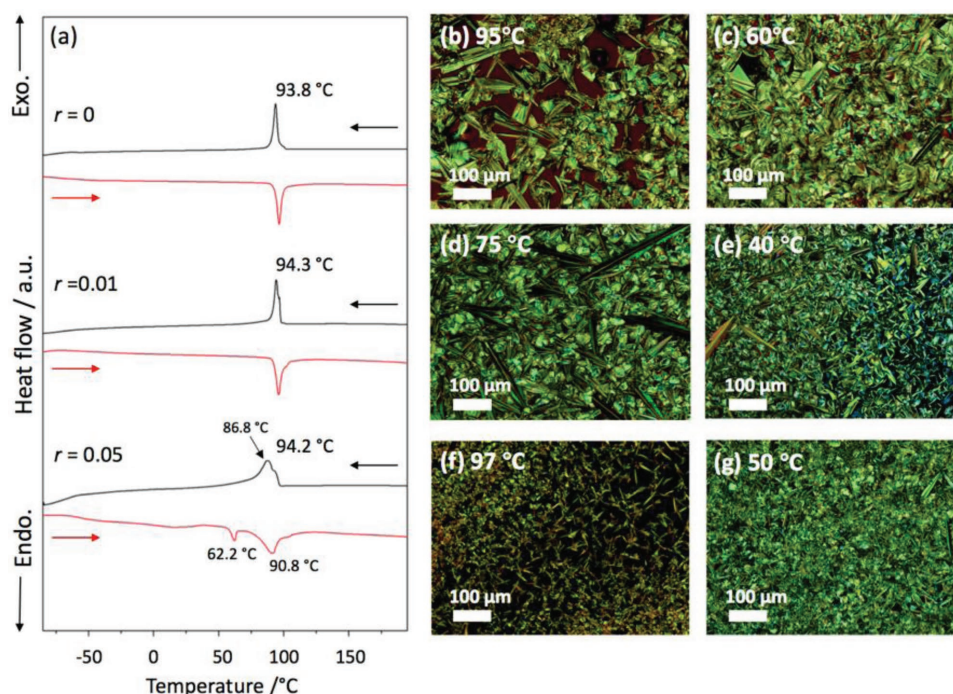


Figure 1. DSC traces ($10\text{ }^{\circ}\text{C min}^{-1}$) and POM images of 4T/PEO4-LiTFSI complexes: a) first cooling scans (indicated by black arrows) and second subsequent heating scans (indicated by red arrows) of 4T/PEO-LiTFSI complexes ($r = 0$, $r = 0.01$, $r = 0.05$), b,c) POM image of pristine 4T/PEO4 ($r = 0$) on cooling from isotropic melt at 95 and 60 °C, d,e) POM image of 4T/PEO4-LiTFSI complex ($r = 0.01$) on cooling from isotropic melt at 75 and 40 °C, and f,g) POM image of 4T/PEO4-LiTFSI complex ($r = 0.05$) on cooling from isotropic melt at 97 and 50 °C (scale bar: 100 μm).

ratios $r = [\text{Li}^+]/[\text{EO}] = 0$ (neat sample), 0.01, and 0.05. We notice that higher blending concentration r results in a more complex structure due to the strong interaction of LiTFSI with the LC molecules and is the subject of a separate investigation.

Figure 1a presents the DSC traces from the first cooling scans and the subsequent second heating scans obtained for the three samples $r = 0$, 0.01, and 0.05. The doping ratio r was set between 0 and 0.05 because ionic conductivity in polyether derivatives generally shows a maximum in the vicinity of 0.05 mol of ions to ethylene oxide unit.^[20] The thermogravimetric analysis (TGA) results shown in Figure S2 (Supporting Information) suggest that both 4T/PEO4 and LiTFSI remain stable within the DSC temperature range. All three samples exhibit stable LC mesophases at room temperature. Pristine compound 4T/PEO4 ($r = 0$) shows a pronounced transition during both cooling and heating processes. The blended complexes, on the other hand, exhibit more complicated thermal behaviors, including multiple phases observed from the small shoulder peak around the transition temperature as well as a monotropic transition in the heating process for $r = 0.05$. A sharp transition temperature appears around 94 °C for all three samples (93.8 °C for $r = 0$, 94.3 °C for $r = 0.01$, and 94.2 °C for $r = 0.05$) suggesting that the addition of LiTFSI does not change the structure and phase of 4T/PEO4. What cannot be neglected, however, is the broadening of the transition peak and the appearance of a shoulder peak (86.8 °C) for sample $r = 0.05$, which suggests that an even more complicated phase shows up and overwhelms the original smectic phase. A higher doping ratio was not adopted due to the possibility that the incorporation of large TFSI anions is antagonistic to an ordered phase and may disturb the in-plane

packing of thiophenes in the smectic layer and therefore destabilize the LC structures.^[10]

The POM images provide a clearer picture toward the process of the phase transition. The bulk material is placed between a piece of glass microscope slide and cover slip. The sample is heated to above the transition temperature at a heating rate of $10\text{ }^{\circ}\text{C min}^{-1}$, the same as the DSC scan rate. A film of several micrometers thick is formed between the microscope slide and cover slip when the sample optically turns black under the polarized light microscope, signifying an isotropic melt. In Figure 1b, the formation of a batonnet texture, typical for a smectic phase, is observed for pristine 4T/PEO4 compound when cooled from isotropic melt at 95 °C. Such a texture is maintained until the sample is cooled down to 60 °C (see Figure 1c) where the texture becomes more uniform, suggesting that the compound has formed a smectic phase. The two blended complexes, on the other hand, exhibit more complicated phase transitions during the cooling process. The complex with $r = 0.01$ also shows a batonnet texture at the beginning of the cooling process, which is then taken over by two coexisting mesophases as shown in Figure 1d. The coexistence of different textures suggests the possibility of multiple mesophases whose transition temperatures are so close that the transition peaks have overlapped, consistent with DSC measurement. As temperature further decreases, the batonnet texture fades while the other more ordered phase becomes the majority at ambient temperature (see Figure 1e). The complex with $r = 0.05$ shows a similar trend to the one with $r = 0.01$. An obvious batonnet texture at the isotropic–smectic transition was observed as shown in Figure 1f, which then also experiences

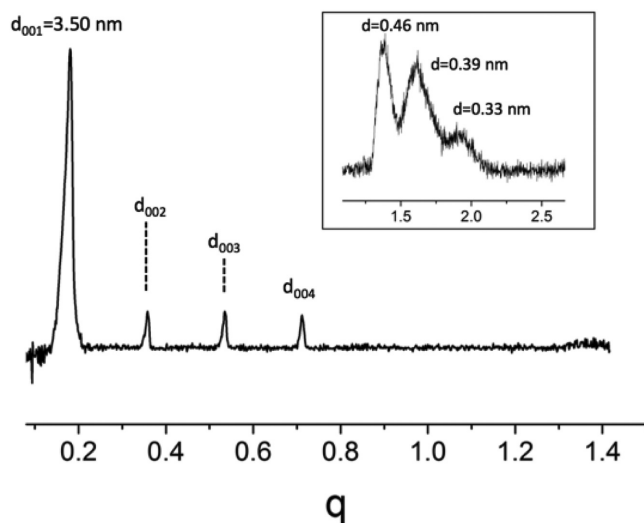


Figure 2. X-ray diffraction pattern of neat 4T/PEO4 compound (bulk) shows smectic phase at ambient temperature.

coexistence with and replacement by a higher ordered phase as temperature decreases (see Figure 1g). At room temperature the complex exhibits a less ordered smectic phase compared to that with $r = 0.01$. Such phenomena can be attributed to the higher doping ratio of LiTFSI that slightly disturbs π - π stacking of oligothiophene thus reducing the degree of chain alignment within the materials.

X-ray diffraction (XRD) was carried out to examine the mesomorphic phase structures of compound 4T/PEO4 and its blended complexes with LiTFSI. **Figure 2** shows the representative XRD pattern for compound 4T/PEO4 as a bulk material at ambient temperature. The four diffraction peaks indexed as (001), (002), (003), and (004) indicate a layer spacing of ≈ 3.5 nm in the smectic phase. The broad peaks in the wide-angle region reflect the molecular arrangement inside each layer with intermolecular distances from 0.33 to 0.46 nm. We assigned these peaks to the π - π stacking of 4T units as they are within the expected range of π - π stacking distance.^[52,53] This result not only supports the existence of an ordered smectic structure with fixed layer distance, but also suggests π stacking between oligothiophene segments might play a role in maintaining such structure, in accordance with the POM images. Later we will show that this conclusion is further supported by MD simulation and GIWAXS measurement. The small-angle X-ray scattering patterns of 4T/PEO4-LiTFSI complexes can be found in Figure S1 (see Supporting Information).

2.3. Self-Assembly Behavior of 4T/PEO4-LiTFSI Thin Film Measured by Temperature-Dependent GIWAXS

To gain more insight into the self-assembly behaviors of 4T/PEO4, we performed temperature-dependent GIWAXS measurement on ≈ 80 nm thin film samples of 4T/PEO4-LiTFSI complexes. The experiments were carried out at different temperatures ranging from 25 to 123 °C to capture the phase transition behavior of 4T/PEO4 revealed by DSC. The samples were equilibrated at each temperature for ≈ 20 min. **Figure 3** shows

exemplary GIWAXS patterns of the three samples ($r = 0, 0.01, 0.05$) at selected temperatures: as-cast sample at 25 °C, high temperature at 123 °C, and annealed sample at 25 °C after cooling back from the first heating cycle. At each selected temperature, the GIWAXS patterns of the three samples appear qualitatively similar. As shown in Figure 3a, for pristine 4T/PEO4 thin film $r = 0$ at 25 °C, we observe narrow and well-defined diffraction peaks ($00h$) in the out-of-plane direction up to the fourth order. This is evidence of a smectic morphology in which the layers are oriented parallel to the substrate with a layer distance of ≈ 3.42 nm, in good agreement with XRD results shown in Figure 2. This observation demonstrates that different fabrication methods do not affect LC structures and molecular alignment for this material. While this smectic morphology is retained in both LiTFSI-blended samples at 25 °C, we observe an increase in the layer spacing distance from 3.42 to 3.48 nm upon introduction of LiTFSI at $r = 0.05$. This observation provides indirect evidence that addition of LiTFSI swells the PEO domains, similar to previous studies on block copolymer-salt and LC-salt complexes.^[54,55] Interestingly, together with the smectic ordering peaks, we also observe two strong elongated peaks near $q_r \approx 1.3$ – 1.5 Å⁻¹ denoted as A and B and other elongated peaks at higher q in Figure 3a,d,g. The A and B peaks originate from the π -stacking interaction of the adjacent 4T units whereas the other elongated peaks are the higher order peaks of A and B. Later we will show that this conclusion is further supported by molecular dynamics simulations. The elongation of these peaks most likely originates from the strong in-plane but rather weak out-of-plane interaction of the π - π stacking units. In other words, the 4T units interact exclusively with other 4T units within the same 2D smectic layer.

As the sample is heated above the transition temperature, the π - π diffraction peaks become notably weak in $r = 0$ sample shown in Figure 3b, and not observable in $r = 0.01$ and $r = 0.05$ samples (see Figure 3e,h). Coinciding with the weakening/disappearing of the π - π interaction peaks, we observe a substantial broadening of the ($00h$) diffraction peaks, indicating a significant loss of smectic ordering above the transition temperature. Our results thus unambiguously indicate that the π - π interaction of the 4T units plays a significant role in controlling the layered structures of 4T/PEO4. Here, it is important to note that at high temperature, all samples are not completely disordered and still maintain weakly layered structures. Upon cooling from above the transition temperature, partial recovery of the ordered smectic phases as well as some new diffraction features are observed as shown in Figure 3c,f,i. Any unmelt molecules remaining after the heating process act as nucleation sites upon cooling and lead to LC phases with different configurations. In particular, we observe a broadening along the azimuthal direction of both π - π stacking peaks and ($00h$) peaks (indicated by the arrows), which is similar to previous reports of oligothiophene/low molecular weight polythiophene thin films.^[56,57] The broadening of the azimuthal breadth of the ($00h$) and π - π stacking peaks for all samples indicates disordering of the 4T units, which induces misalignment of the smectic domains. This observation provides further evidence that π - π interaction dictates the molecular ordering of 4T/PEO4.

To show the temperature dependence of the structure in a more quantitative manner, we show in **Figure 4** the vertical

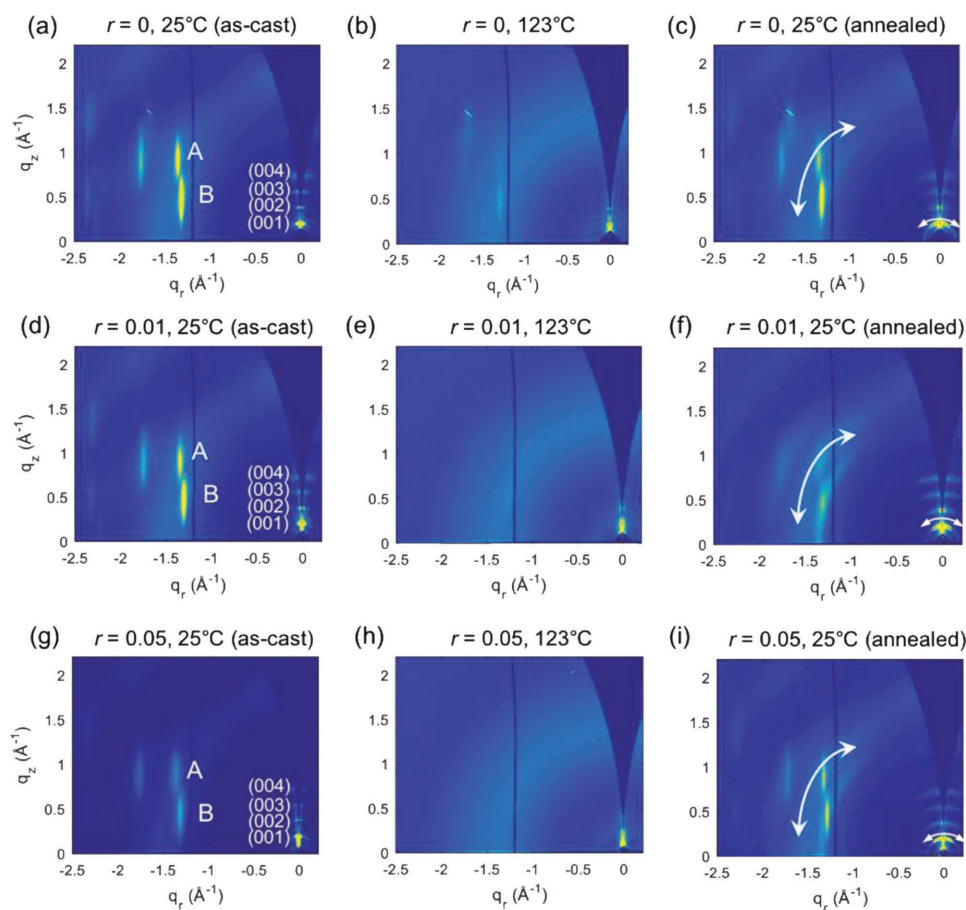


Figure 3. Representative geometrically corrected GIWAXS patterns of 4T/PEO4-LiTFSI complex thin film at selected temperatures during heating and cooling processes a–c) $r = 0$, d–f) $r = 0.01$, and g–i) $r = 0.05$. Thin film of pristine 4T/PEO4 compound ($r = 0$) at (a) 25 °C (as-cast), (b) 123 °C (during heating), and (c) 25 °C (after annealed). Thin film of 4T/PEO4-LiTFSI complex ($r = 0.01$) at (d) 25 °C (as-cast), (e) 123 °C (during heating), and (f) 25 °C (after annealed). Thin film of 4T/PEO4-LiTFSI complex ($r = 0.05$) at (g) 25 °C (as-cast), (h) 123 °C (during heating), and (i) 25 °C (after annealed). All samples were annealed at each temperature for 20 min to reach equilibrium. The arrows in (c), (f), and (i) indicate the peak broadening along the azimuthal direction.

linecuts from the GIWAXS patterns of the three samples at all temperatures during the heating and cooling processes. The linecuts of all three complexes below the transition temperature during both the heating and cooling processes consist of sharp diffraction peaks at $q/q^* = 2, 3$, and 4 representing (002), (003), and (004), again confirming a well-ordered smectic morphology at room temperature. As temperature increases, all the samples undergo an order–disorder transition, indicated by the broadening of the scattering peaks in the vicinity of 100 °C, where a smectic–isotropic transition takes place shown by optical microscope. It is worth mentioning that there is a subtle difference among the transition temperatures for each sample, with 106–114 °C for pristine 4T/PEO4, 96–106 °C for $r = 0.01$ sample, and 87–96 °C for $r = 0.05$ sample. The decrease in transition temperature with increasing blend ratio is in good agreement with DSC measurements.

As mentioned above, the π – π stacking interaction between 4T units has made the LC phases of 4T/PEO4 much more complicated than the commonly observed smectic A (SmA) or smectic C (SmC) phases. Highly ordered smectic phases such as SmF, SmG, SmI, SmJ, etc., with a long molecular axis are

not only tilted with respect to layer surface, but also toward one side or one apex have been identified after SmC phases.^[58] With GIWAXS patterns closely resembling the intermediate tilted phase of a fatty acid monolayer,^[59] we conclude that the smectic phase the 4T/PEO4 exhibits belongs to is a highly ordered smectic phase.

2.4. Self-Assembly Behavior of 4T/PEO4 Studied by Molecular Dynamics Simulation

To provide complementary insights to the experimental results, we employ all-atom (AA) MD simulations to study the self-assembly behavior of 4T/PEO4 as a function of temperature. Specifically, we adopted the AA MD force field potential developed by Marcon and Raos (MR) as it is known to capture experimental density, crystal structure, and heat of sublimation of oligothiophenes.^[60,61] However, the MR force field does not describe the PEO potentials, which are required to simulate 4T/PEO4. Since the nonbonded interactions in MR model are obtained from optimized potentials for liquid simulations—all

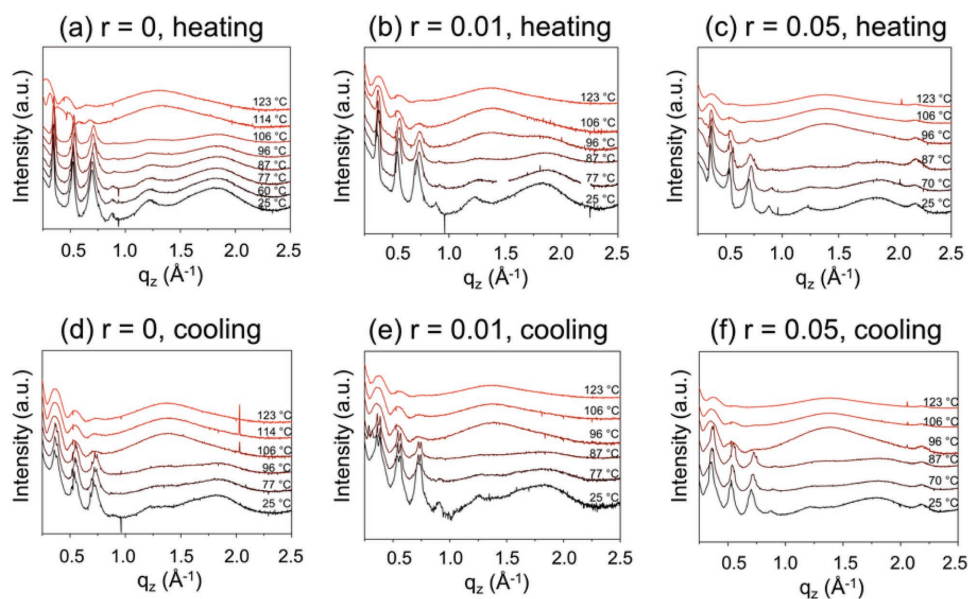


Figure 4. Vertical linecuts of (00h) spot sequence for 4T/PEO4-LiTFSI complexes at different temperatures for a,d) $r = 0$, b,e) $r = 0.01$, and c,f) $r = 0.05$ during each heating and cooling processes. The curves are vertically translated for better comparison.

atom force field (OPLS-AA),^[62,63] we use it to define the missing potential parameters. The charges on the terminal carbon attached to 4T on PEO4 unit were modified to maintain charge neutrality. The bonded parameters were refined by fitting them to results from ab initio density functional theory (DFT) calculations. The details of fitting and the parameters used in the atomistic simulation are given in the Supporting Information. We use LAMMPS molecular dynamics simulation package^[64] with general-purpose graphical processing units (GPGPU) enabled to accelerate van der Waals and particle-particle particle-mesh (PPPM) calculations.^[64,65] Unless otherwise stated, all simulations were carried out in a triclinic periodic box at constant temperature and standard pressure (NPT ensemble), using a Nosé Hoover thermostat and barostat. The timestep for all simulations was 1 fs.

Our attempts to directly self-assemble this system from the melt state via AA simulations proved ineffective due to the considerable computational challenges associated with the slow kinetics of this process. To circumvent this limitation, we used a suitably calibrated coarse-grained (CG) model, an approach that has been proven effective in describing the self-assembly of similar systems.^[66,67] For 4T/PEO4, our CG model represents each thiophene ring by a single spherical bead,^[68] and multiple aliphatic segments by a single bead depending on the specific chemistry (see Figure 5a).^[69] We parameterized bonded potentials to match the bond and angle distribution from AA simulations of 4T/PEO4 using a relative entropy framework.^[70] Further details of the mapping procedure and fitted parameters of the CG model are provided in the Supporting Information.

The CG simulation started from an amorphous 400-molecule system, shown in Figure 5a, which was equilibrated for 5 ns at 625 °C, a high enough temperature to ensure complete isotropization. The amorphous system was then cooled at a constant rate of 50 °C ns⁻¹ to 27 °C, and then equilibrated at the

final temperature for 10 ns. In agreement with XRD results of the bulk material and GIWAXS results of thin films, the final equilibrated structure obtained is smectic, where 4T units are tilted at an angle $25 \pm 3^\circ$ to the layer stacking direction. The self-assembled CG structure at 27 °C provides a good initial guess for generating the LC AA structure. We used a reverse coarse-grained technique to replace the CG beads with their atomistic representation as implemented by Marrink and co-workers.^[71] The resulting AA system was relaxed at 27 °C for 10 ns. Note that the equilibrated AA structure (Figure 5a) provides information on the thiophene ring packing not available in the CG model.

Figure 5b shows a representative arrangement of six adjacent 4T units within a smectic layer at 27 °C. We observe that the 4T units self-assemble into a typical herringbone packing comparable to the P2₁/c crystal structure of pure 4T reported by Campione et al.,^[72] indicating that the 4T self-assembly drives the ordering of the smectic structure of 4T/PEO4. Unlike the CG smectic phase, the AA structure does not reveal any ordering in the PEO domains, showing instead that PEO chains from adjacent layers tend to interdigitate.

To compare the simulated structure to GIWAXS results, we calculate the structure factor^[73] for the thiophene rings, $S(\mathbf{q}) = |\sum_n \exp(i\mathbf{q} \cdot \mathbf{r}_n)|^2$, where \mathbf{r}_n is the center of mass of each non-hydrogen atom in thiophene ring. The 2D $S(\mathbf{q})$ shown in Figure 5c results from averaging the q_x and q_y components along circles of constant $q_r = \sqrt{q_x^2 + q_y^2}$. The simulated GIWAXS pattern shows key similarities to the experimental one shown in Figure 3a: (i) the (00h) peaks identify a smectic structure with calculated layer thickness of 3.41 nm, and (ii) the two peaks originating from the herringbone structure denoted as A and B. In Figure 5b, these two peaks represent the alignment between the homo-tilts with 0.39 nm spacing and hetero-tilts with 0.44 nm spacing in the herringbone packing, respectively (the spacing is the mean distance between thiophene ring centers of mass).

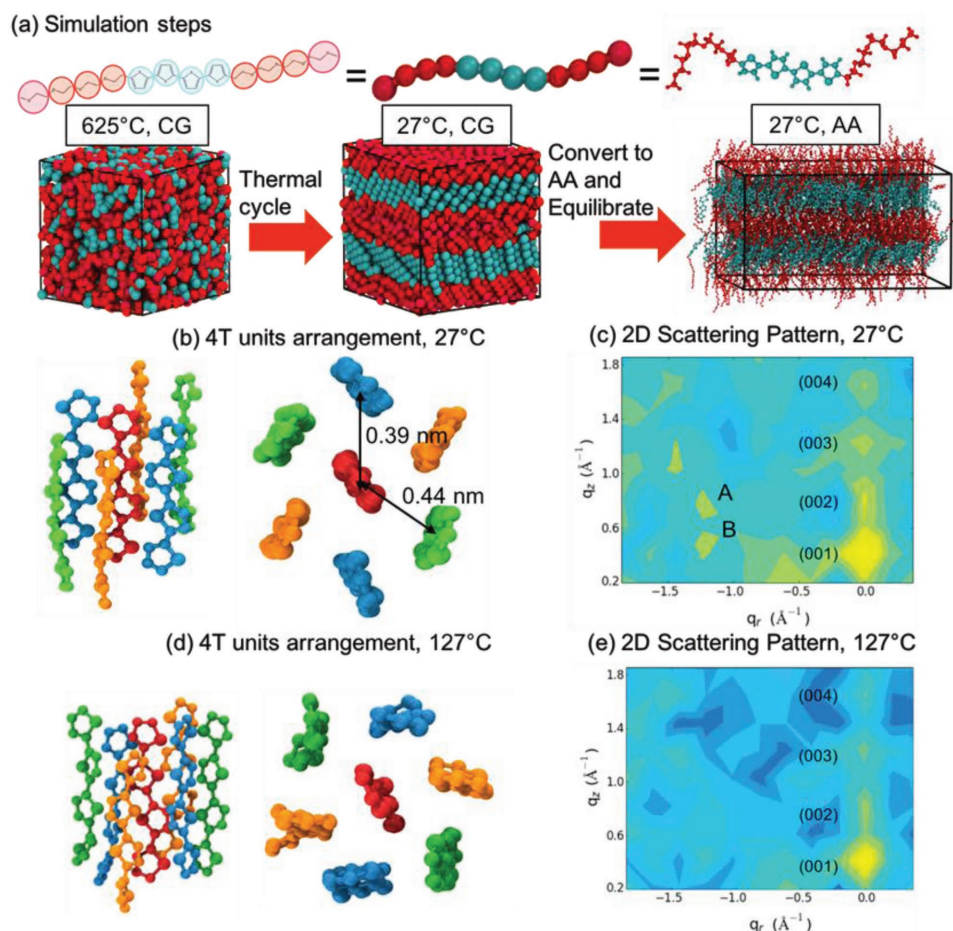


Figure 5. a) Simulation steps to capture the AA structure of 4T/PEO4 at 27 °C. The thiophene rings are shown in cyan, the PEO units are shown in red, and hydrogens are omitted for clarity. Herringbone packing of the thiophene units at b) 27 and d) 127 °C is shown in perpendicular and parallel views to the thiophene principal axis, with 4T units given different colors and PEO4 chains omitted for clarity. c,e) Average 2D structure factor of the thiophene rings at 27 and 127 °C, respectively.

To simulate the morphology change of 4T/PEO4 with temperature, we heat the system from 37 to 187 °C in 10 °C increments. At each temperature the system is annealed for 10 ns in attempt to achieve equilibrium before taking the next step. Figure 5d,e shows the arrangement of 4T units and the corresponding GIWAXS patterns at $T = 127$ °C which is above the disordering transition temperature of 4T/PEO4. At $T = 127$ °C, the top view of the 4T units shows a considerable twisting/bending compared to that at 27 °C, leading to a significant loss of the π - π interaction between the 4T units. Accordingly, the simulated GIWAXS pattern in Figure 5e shows no evidence of π - π stacking peaks (with only weaker smectic (00h) peaks persisting), which is again in agreement with our experimental results presented in Section 2.3.

2.5. Structure Evolution of 4T/PEO4 as a Function of Temperature: A Quantitative Analysis from Experiment and Simulation

To further elucidate the self-assembly behavior of 4T/PEO4, we calculate (i) the smectic layer spacing, (ii) the π - π stacking distance, and (iii) the full-width at half-maximum (FWHM)

of the smectic peaks as a function of temperature from both experimental GIWAXS data and simulation. We also examine the conformational change in PEO4 with temperature. To compute the smectic layer spacing and FWHM from experiment, we choose to analyze the (002) peak from GIWAXS data for having a strong signal and minimal background scattering from the direct beam. For the π - π stacking distance, we only show data from peak B since either peak A or B yields similar trends. Moreover, we choose to analyze the structural evolution only during the heating cycle. This is because of the challenges posed by the cooling data: in the experiments, the GIWAXS peak shape analysis is nontrivial given the appearance of extra peaks that overlap with the original smectic and π - π stacking peaks; and in the AA simulations, the disorder-to-order process is prone to kinetic trapping, rendering unreliable result obtained from any practicable cooling rates. Finally, we choose to conduct simulations for the $r = 0$ sample only due to the similarity of the self-assembly behaviors of the $r = 0$, 0.01, and 0.05 samples as indicated by experimental GIWAXS patterns.

As shown in Figure 6a, a rapid decrease in lamellar distance is observed for all samples with increasing temperature above 47 °C for both experiment and simulation. However, at

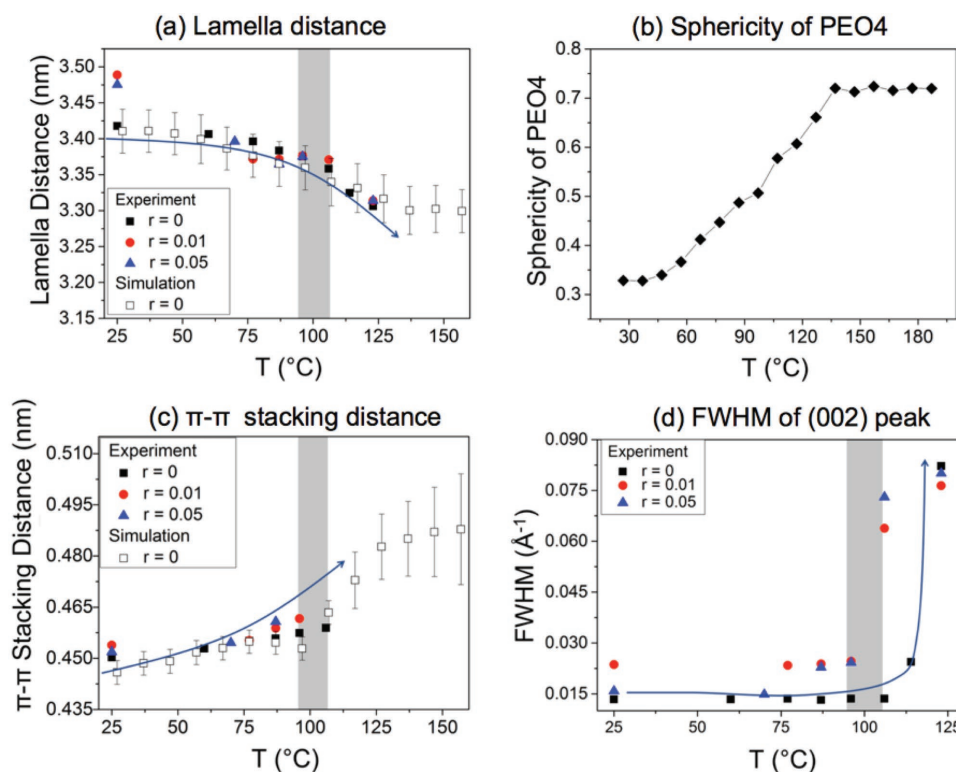


Figure 6. a) Temperature dependence of lamella stacking distance, b) sphericity of PEO4 chains from simulation, c) π - π stacking distance, and d) FWHM of the (002) peaks extracted from experimental GIWAXS data of 4T/PEO4-LiTFSI complexes of $r = 0$, 0.01, and 0.05. The corresponding simulation results for $r = 0$ sample are also shown in (a) and (c). The simulated sphericity of PEO4 chains as a function of temperature is shown in (b). The gray-shaded areas represent order-disorder transition region.

137 °C the lamella distance becomes constant at 3.3 nm. To further probe the origins of the variation of lamella distance with temperature, we also calculate the tilt angle of the thiophene and observe a slight increase from $25 \pm 3^\circ$ to $28 \pm 4^\circ$ between 27 and 47 °C. This change in the tilt angle is accompanied by formation of $P2_1/a$ symmetry in the sample and a decrease of lamella thickness with increasing temperature. Furthermore, for the PEO4 units we calculate the sphericity (S) defined by $S = 3(\lambda_2 + \lambda_3)/2$, where the λ_1 , λ_2 , and λ_3 are eigenvalues of the inertial tensor and $\lambda_1 > \lambda_2 > \lambda_3$;^[74] for a stiff rod-like chain $S \approx 0$ and for a random coil $S \rightarrow 1$. The sphericity of PEO4 chains increases slightly ($S = 0.32 \rightarrow 0.33$) from 27 to 47 °C and increases rapidly from 57 to 137 °C, plateauing at $S \approx 0.72$ thereafter, as shown in Figure 6b. This rapid increase in sphericity above 57 °C originates from melting of PEO4 chains which contributes to the thinning of the lamella.^[75] This persistence of smectic order despite the disordering of the PEO4 units again shows the stabilizing effect of the π - π interactions. Both experimental and simulation results in Figure 6a,b indicate that the PEO4 melting (and the concomitant shrinkage of the lamellar spacing) is a continuous order transition and thus does not reflect the transition at 93.8 °C observed in DSC.

We characterize the 2D order in real space by calculating the 2D radial distribution function (in the XY plane) of the center of mass of the thiophene rings with homo-tilts and $r_z < 0.4$ nm, where r_z is the distance between the center of mass of the rings parallel to lamella. Figure 6c depicts the changes in r_z

as a function of temperature for both experiment and simulation. It shows that r_z slightly increases from 0.44 to 0.45 nm between 27 and 97 °C, but increases significantly between 97 and 137 °C. This transition around 107 °C is due to the loss of the herringbone symmetry, and hence the loss of optimal π - π interactions and the 2D ordering of thiophene units. Figure 6d shows the FWHM of the (002) peak as a function of temperature. The order-disorder transition is clearly indicated by the abrupt increase in the FWHM around 100 °C. In each figure, the gray-shaded area depicts the order-disorder transition regime of the samples.

2.6. Implication of 4T/PEO4-LiTFSI Self-Assembly on Ion Transport

The ionic conductivity of 4T/PEO4-LiTFSI thin films is measured by EIS using interdigitated gold electrodes devices (IDEs) as shown in Figure 7a. IDEs are used in order to enhance signal-to-noise ratio in highly resistive thin films.^[76,77] Due to the geometry of IDE, the ionic conductivity reported in our work is in-plane conductivity, or conductivity in the direction parallel to the substrate. In fact, in the smectic phases the 4T/PEO4-LiTFSI complexes exhibit homeotropic alignment, indicating the formation of 2D ion-conductive pathways parallel to the surface of substrate. Figure 7b depicts the temperature-dependent ionic conductivity of the two samples $r = 0.01$ and

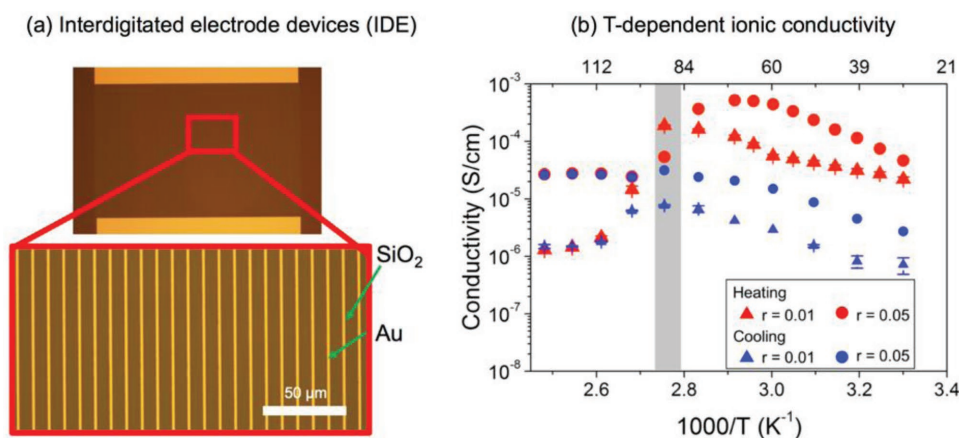


Figure 7. a) Optical microscope image of an interdigitated gold electrode device (IDE) used for ionic conductivity measurement, and b) ionic conductivities of LiTFSI-blended 4T/PEO4 thin film at $r = 0.01$ and $r = 0.05$ as a function of temperature during heating and cooling processes. The gray-shaded area indicates the order–disorder transition regime.

$r = 0.05$ during heating and cooling cycles. In the complexes, ions propagate through segmental motion of PEO chains. For both samples, the conductivity appears qualitatively similar, consistent with similar temperature-dependent morphology suggested by GIWAXS measurement above. From $r = 0.01$ to 0.05 , we observe a significant improvement in conductivity due to the increase in ionic carrier concentration. During the first heating cycle below the transition temperature, the ionic conductivity monotonically increases with temperature, consistent with thermally activated ionic transport behavior of electrolytes.^[78]

The maximum conductivity is $\approx 1.9 \times 10^{-4} \text{ S cm}^{-1}$ for $r = 0.01$ sample (at 90°C), and $5.2 \times 10^{-4} \text{ S cm}^{-1}$ for $r = 0.05$ sample (at 70°C), which are comparable or even superior to those of nanosegregated ionic LCs.^[17,18,26,54,79–81] 2D lamellar system also has more flexibility in device design in which allows the transport of lithium ions within the layers along more directions compared to 1D cylindrical structures. What's more, these conductivity values from our material are achieved at relatively lower temperatures, endowing more practicality and processability to 4T/PEO4. We believe that the high ionic conductivity of 4T/PEO4-LiTFSI thin films originates from the formation of the highly ordered smectic layers and thus efficient 2D transport pathways in the direction parallel to the device substrate as suggested by GIWAXS measurements. However, at around 100°C where the order–disorder transition takes place, as indicated by the gray-shaded area in Figure 7b, we observe a substantial drop in ionic conductivity. This is most likely because the layered structures and ion transport channels are disturbed at this temperature as indicated by the significant broadening of the $(00h)$ layering peaks in GIWAXS measurement. This behavior has already been reported for a number of columnar and smectic ionic LCs.^[18,26,54,79–81] Finally, upon cooling the samples from above the transition temperature to room temperature, the ionic conductivity does not recover to its initial value, which is also consistent with GIWAXS measurements suggesting that the conductivity loss is caused by the misalignment of the smectic layers due to local and partial crystallization of 4T/PEO4 upon cooling as well as larger grain size obtained due to shrunken layer structure and expanded π – π stacking.

Furthermore, the same measurements were run for another two cycles afterward, and the data followed exactly the second trend where the ionic conductivity before and after heating/cooling treatment remains the same. This behavior suggests that the LC mesophases and molecular alignments are stable.

3. Conclusion

In summary, we have performed a systematic study on the structure and self-assembly of newly synthesized conjugated LC compound 4T/PEO4 upon blending with LiTFSI in connection with its ionic conduction characteristics. For the first time modeling has played an important role in guiding the design and understanding the self-assembly behaviors of the conducting material. We believe that the method using simulation to interpret experimental data is an elegant approach toward understanding the self-assembly and transport behavior of soft materials in general. For all three blend ratios, the compounds exhibited a highly ordered smectic phase due to segregation between immiscible aromatic and aliphatic segments as well as π – π stacking of thiophene rings, forming efficient 2D channels for ion transport. EIS measurements on 4T/PEO4-LiTFSI samples showed remarkable ion transport behavior with the highest conductivity of $5.2 \times 10^{-4} \text{ S cm}^{-1}$ at 70°C and $r = 0.05$. Temperature-dependent GIWAXS measurements and molecular dynamic simulations indicated that upon heating the samples from ambient temperature to above the isotropization temperature, a significant loss in π – π interaction and smectic order was observed, which led to a significant drop in ionic conductivity due to disruption of the ordered smectic phase and ion transport pathways. Additionally, the conductivity became lower than the initial state upon cooling to ambient temperature due to the disruption of 2D ion transport channels.

The incorporation of oligothiophene not only provides π – π interaction which helps the formation of 2D ion transport channel, but also endows electron conducting capability to this compound and makes it an even more promising material with mixed ionic/electronic conduction characteristics. It is known that π -conjugated LCs have great potential as organic

semiconductors,^[3,82–84] field-effect transistors,^[85–90] and electroluminescence devices^[91,92] because of their flexibility, ease of processability into thin films, and charge carrier transport ability. In fact, Kato and co-workers have already realized this idea by synthesizing a molecule consisting of terthienylphenylcyanoethylene mesogen and imidazolium triflate moiety which successfully showed electrochromic properties; however, no electronic conductivity results were reported.^[93] With easily attainable ordered structures and a relatively lower viscosity compared to conjugated polymers, 4T/PEO4 has significant potential of exhibiting mixed ionic–electronic conductivity and is the object of ongoing investigations.

4. Experimental Section

Materials and Synthesis: All reagents and solvents were purchased from Sigma-Aldrich, AK Scientific, or one click chemistry, and used as received unless otherwise noted. Anhydrous tetrahydrofuran (THF) was freshly distilled from sodium and benzophenone prior to use. N-bromosuccinimide (NBS) was recrystallized in water and stored in a refrigerator before use. The synthetic procedure and characterization of 4T/PEO4 are provided in the Supporting Information.

Preparation of 4T/PEO4-LiTFSI Blend Samples: Solutions of 4T/PEO4 and LiTFSI (Sigma Aldrich, battery grade) were prepared separately by dissolving the materials in anhydrous THF at a concentration of 10 mg mL^{−1} each and fully shaken using a vortexer before mixing. 4T/PEO4 and LiTFSI solutions were then mixed at the appropriate ratios to achieve the concentrations $r = [\text{Li}^+]/[\text{EO}]$. DSC, POM images, and XRD were taken on bulk 4T/PEO4-LiTFSI complexes prepared by slow evaporation of the mixed 4T/PEO4-LiTFSI solution at 80 °C followed by drying under vacuum for 24 h at 80 °C.

Small-angle X-ray scattering (SAXS), GIWAXS, and ion conductivity measurements were performed on 4T/PEO4 thin films spin-cast from the mixed solution at 1000 rpm for 2 min. The film thickness of all thin film samples is ≈80 nm as confirmed by spectroscopic ellipsometry.

Characterization Methods: NMR: ¹H and ¹³C NMR spectra were recorded on a Varian INOVA 400 and a MERCURY 300 spectrometers. Chemical shifts were quoted relative to the residual protons of the deuterated solvents CDCl₃ ($\delta = 7.26$ for ¹H and $\delta = 77.36$ for ¹³C). The multiplicity was characterized by the following abbreviations: s-singlet, d-doublet, t-triplet, q-quartet, m-multiplet.

Differential Scanning Calorimetry: DSC measurements were performed on a Q 2000 from TA Instruments at a scanning rate of 10 °C min^{−1} within temperature range from −90 to 250 °C. The phase transition temperatures were determined as the peak positions in the DSC traces due to broadness of the transition peaks.

Polarized Optical Microscope: An Olympus BX51 polarizing optical microscope equipped with a Mettler FP 82 HT hot stage was used for visual observation of optical textures at different temperatures.

X-Ray Diffraction and Small-Angle X-Ray Scattering: XRD patterns were obtained using Bruker D8 Advance ECO powder diffractometer with Cu K α radiation $\lambda = 1.54$ Å. SAXS patterns were obtained using Rigaku SmartLab X-ray diffractometer with Cu K α radiation $\lambda = 1.54$ Å.

Grazing-Incidence Wide-Angle X-Ray Scattering: Temperature-dependent GIWAXS measurements were performed at beamline 8-ID-E of the Advanced Photon Source, Argonne National Laboratory with 10.86 keV ($\lambda = 1.1416$ Å) synchrotron radiation. The temperature of the samples was varied from room temperature up to 130 °C using a Linkam HFSX350-GI stage. Samples were measured inside a low vacuum chamber (10^{−3} mbar) to minimize concerns about radiation damages, samples' moisture uptake, and extraneous scattering from ambient air. The measurement time was chosen to be 3 s frame^{−1}. For each sample, three data sets were taken from three adjacent spots on the sample and then summed in order to enhance the signal-to-noise ratio. The samples were tilted at an angle of incidence of 0.14° with respect to the incoming

beam, which is above the estimated critical angle of sample ($\approx 0.13^\circ$) but below the critical angle of the Si substrates ($\approx 0.17^\circ$) in order to probe the whole film thickness. The scattering signal was recorded with a Pilatus 1MF pixel array detector (pixel size = 172 μm) positioned 228 mm from the sample. Each data set was stored as a 981 × 1043 32-bit tiff image with 20-bit dynamic range. The Pilatus detector has rows of inactive pixels at the border between detector modules. In order to fill these gaps, after each measurement the detector was moved to a new vertical direction and the measurement on each spot was repeated, then the gaps were filled by combining the data from two detector positions. The signals were reshaped and output as intensity maps in q_z versus q_r ($=\sqrt{q_x^2 + q_y^2}$) space. We also performed detector nonuniformity, detection efficiency, the polarization effect, and solid-angle variation for each image. All the GIWAXS data processing and extraction were executed using the GIXSGUI package for MATLAB.^[94]

Peak shape analysis was performed on wedge cuts taken with an angular breadth of 2°. Each wedge cut was first fit to an empirical baseline function to enable the subtraction of the background intensity and amorphous scattering. The background-subtracted wedge cut was then fit to a Voigt function to extract the peak position and the FWHM of the reflections of interest. More details of peak shape analysis can be found elsewhere.^[95]

Conductivity Measurements: EIS conductivity measurements were performed on samples fabricated on top of custom-built interdigitated gold electrode devices (IDE) using a Gamry 600+ Potentiostat inside a nitrogen-filled glovebox. Prior to EIS measurement, the excess amount of materials on the electrode pads was scraped away to make electrical connection from the potentiostat to the sample. The electrical connection was made using two-probe manipulators (Semiprobe Inc.). The EIS characterization was performed from 1 MHz to 0.1 Hz with an oscillatory peak potential of 50 mV. EIS measurement was carried out at different temperature controlled by a miniature benchtop heater controller (Omega Engineering Inc.). The collected impedance data were then fit to the appropriate equivalent circuit in order to extract the sample ionic resistance R_{ion} and then ionic conductivity according to the following equation^[76]

$$\sigma = \frac{1}{R} \frac{d}{l(N-1)h}$$

l : the length of gold electrode, 1000 μm

d : distance between adjacent electrode teeth, 8 μm

N : number of gold electrodes, 160

R : ion resistance

h : total thickness of the sample, 80 nm.

Supporting Information

Supporting Information is available from the Wiley Online Library or from the author.

Acknowledgements

Z.L., B.X.D., and M.M. contributed equally to this work. This work was supported by National Science Foundation (DMREF-1629369). The authors would like to acknowledge Prof. Detlef-M. Smilgies for advice and guidance on GIWAXS data analysis. This work made use of the Cornell Center for Materials Research Shared Facilities which are supported through the NSF MRSEC program (DMR-1719875). This research also used the resources of the Advanced Photon Source, an Office of Science User Facility operated for the U.S. Department of Energy (DOE) by Argonne National Laboratory under Contract No. DE-AC02-06CH11357.

Conflict of Interest

The authors declare no conflict of interest.

Keywords

ionic conductivity, liquid crystal, oligothiophene, π - π interactions, self-assembly

Received: July 29, 2018

Revised: October 13, 2018

Published online: November 14, 2018

- [1] G. W. Gray, J. W. G. Goodby, *Smectic Liquid Crystals- Textures and Structures*, Lenard Hill, Glasgow, UK **1984**.
- [2] D. Demus, J. Goodby, G. W. Gray, H. W. Spiess, V. Vill, *Handbook of Liquid Crystals*, Wiley VCH, Weinheim, Germany **1998**.
- [3] W. Pisula, M. Zorn, J. Y. Chang, K. Müllen, R. Zentel, *Macromol. Rapid Commun.* **2009**, *30*, 1179.
- [4] I. W. Hamley, *Angew. Chem., Int. Ed.* **2003**, *42*, 1692.
- [5] T. Kato, N. Mizoshita, K. Kishimoto, *Angew. Chem., Int. Ed.* **2006**, *45*, 38.
- [6] T. Kato, *Science* **2002**, *295*, 2414.
- [7] R. L. Kerr, S. A. Miller, R. K. Shoemaker, B. J. Elliott, D. L. Gin, *J. Am. Chem. Soc.* **2009**, *131*, 15972.
- [8] T. Kato, *Angew. Chem., Int. Ed.* **2010**, *49*, 7847.
- [9] B. R. Wiesenauer, D. L. Gin, *Polym. J.* **2012**, *44*, 461.
- [10] J. Sakuda, E. Hosono, M. Yoshio, T. Ichikawa, T. Matsumoto, H. Ohno, H. Zhou, T. Kato, *Adv. Funct. Mater.* **2015**, *25*, 1206.
- [11] S. Sergeyev, W. Pisula, Y. H. Geerts, *Chem. Soc. Rev.* **2007**, *36*, 1902.
- [12] M. O'Neill, S. M. Kelly, *Adv. Mater.* **2011**, *23*, 566.
- [13] C. Tschierske, *J. Mater. Chem.* **2001**, *11*, 2647.
- [14] G. H. Mehl, *Angew. Chem., Int. Ed.* **2005**, *44*, 672.
- [15] C. Tschierske, *Annu. Rep. Prog. Chem., Sect. C: Phys. Chem.* **2001**, *97*, 191.
- [16] C. Ruiz, E. M. García-Frutos, G. Henrich, B. Gómez-Lor, *J. Phys. Chem. Lett.* **2012**, *3*, 1428.
- [17] H. Shimura, M. Yoshio, A. Hamasaki, T. Mukai, H. Ohno, T. Kato, *Adv. Mater.* **2009**, *21*, 1591.
- [18] M. Yoshio, T. Mukai, H. Ohno, T. Kato, *J. Am. Chem. Soc.* **2004**, *126*, 994.
- [19] B. Soberats, M. Yoshio, T. Ichikawa, X. Zeng, H. Ohno, G. Ungar, T. Kato, *J. Am. Chem. Soc.* **2015**, *137*, 13212.
- [20] T. Ohtake, K. Ito, N. Nishina, H. Kihara, H. Ohno, T. Kato, *Polym. J.* **1999**, *31*, 1155.
- [21] T. Ohtake, Y. Takamitsu, K. Ito-Akita, K. Kanie, M. Yoshizawa, T. Kato, *Macromolecules* **2000**, *33*, 8109.
- [22] K. Kishimoto, T. Suzawa, T. Yokota, T. Mukai, H. Ohno, T. Kato, *J. Am. Chem. Soc.* **2005**, *127*, 15618.
- [23] Y. Iinuma, K. Kishimoto, Y. Sagara, M. Yoshio, T. Mukai, I. Kobayashi, H. Ohno, T. Kato, *Macromolecules* **2007**, *40*, 4874.
- [24] M. Yoshio, T. Mukai, K. Kanie, M. Yoshizawa, H. Ohno, T. Kato, *Chem. Lett.* **2002**, *31*, 320.
- [25] T. Ichikawa, M. Yoshio, A. Hamasaki, S. Taguchi, F. Liu, X. Zeng, G. Ungar, H. Ohno, T. Kato, *J. Am. Chem. Soc.* **2012**, *134*, 2634.
- [26] T. Ichikawa, M. Yoshio, A. Hamasaki, T. Mukai, H. Ohno, T. Kato, *J. Am. Chem. Soc.* **2007**, *129*, 10662.
- [27] A. E. Frise, T. Ichikawa, M. Yoshio, H. Ohno, S. V. Dvinskikh, T. Kato, I. Furó, *Chem. Commun.* **2010**, *46*, 728.
- [28] T. Ichikawa, M. Yoshio, A. Hamasaki, J. Kagimoto, H. Ohno, T. Kato, *J. Am. Chem. Soc.* **2011**, *133*, 2163.
- [29] R. D. Costa, F. Werner, X. Wang, P. Grönninger, S. Feihl, F. T. U. Kohler, P. Wasserscheid, S. Hibler, R. Beranek, K. Meyer, D. M. Guldi, *Adv. Energy Mater.* **2013**, *3*, 657.
- [30] A. Abate, A. Petrozza, G. Cavallo, G. Lanzani, F. Matteucci, D. W. Bruce, N. Houbenov, P. Metrangolo, G. Resnati, *J. Mater. Chem. A* **2013**, *1*, 672.
- [31] N. Yamanaka, R. Kawano, W. Kubo, N. Masaki, T. Kitamura, Y. Wada, M. Watanabe, S. Yanagida, *J. Phys. Chem. B* **2007**, *111*, 4763.
- [32] D. Högberg, B. Soberats, S. Uchida, M. Yoshio, L. Kloo, H. Segawa, T. Kato, *Chem. Mater.* **2014**, *26*, 6496.
- [33] D. Högberg, B. Soberats, R. Yatagai, S. Uchida, M. Yoshio, L. Kloo, H. Segawa, T. Kato, *Chem. Mater.* **2016**, *28*, 6493.
- [34] T. Kato, M. Yoshio, T. Ichikawa, B. Soberats, H. Ohno, M. Funahashi, *Nat. Rev. Mater.* **2017**, *2*, 17001.
- [35] V. Percec, *J. Chem. Soc., Perkin Trans.* **1994**, *16*.
- [36] K. Hoshino, K. Kanie, T. Ohtake, T. Mukai, M. Yoshizawa, S. Ujiie, H. Ohno, T. Kato, *Macromol. Chem. Phys.* **2002**, *203*, 1547.
- [37] K. Goossens, K. Lava, C. W. Bielawski, K. Binnemans, *Chem. Rev.* **2016**, *116*, 4643.
- [38] M. Yoshizawa, T. Mukai, T. Ohtake, K. Kanie, T. Kato, H. Ohno, *Solid State Ionics* **2002**, *154*, 779.
- [39] F. J. M. Hoeben, P. Jonkheijm, E. W. Meijer, A. P. H. J. Schenning, *Chem. Rev.* **2005**, *105*, 1491.
- [40] J. A. A. W. Elemans, A. E. Rowan, R. J. M. Nolte, *J. Mater. Chem.* **2003**, *13*, 2661.
- [41] T.-Q. Nguyen, R. Martel, P. Avouris, M. L. Bushey, L. Brus, C. Nuckolls, *J. Am. Chem. Soc.* **2004**, *126*, 5234.
- [42] L. L. Miller, K. R. Mann, *Acc. Chem. Res.* **1996**, *29*, 417.
- [43] D. D. Graf, J. P. Campbell, L. L. Miller, K. R. Mann, *J. Am. Chem. Soc.* **1996**, *118*, 5480.
- [44] D. D. Graf, R. G. Duan, J. P. Campbell, L. L. Miller, K. R. Mann, *J. Am. Chem. Soc.* **1997**, *119*, 5888.
- [45] X.-C. Li, H. Sirringhaus, F. Garnier, A. B. Holmes, S. C. Moratti, N. Feeder, W. Clegg, S. J. Teat, R. H. Friend, *J. Am. Chem. Soc.* **1998**, *120*, 2206.
- [46] G. Barbarella, M. Zambianchi, A. Bongini, L. Antolini, *Adv. Mater.* **1992**, *4*, 282.
- [47] G. Barbarella, M. Zambianchi, L. Antolini, P. Ostojia, P. Maccagnani, A. Bongini, E. A. Marseglia, E. Tedesco, G. Gigli, R. Cingolani, *J. Am. Chem. Soc.* **1999**, *121*, 8920.
- [48] G. Barbarella, M. Zambianchi, A. Bongini, L. Antolini, *Adv. Mater.* **1993**, *5*, 834.
- [49] S. Suzuki, K. Honda, R. Azumi, *J. Am. Chem. Soc.* **2002**, *124*, 12200.
- [50] H. Sirringhaus, P. J. Brown, R. H. Friend, M. M. Nielsen, K. Bechgaard, B. M. W. Langeveld-Voss, A. J. H. Spiering, R. A. J. Janssen, E. W. Meijer, P. Herwig, **1999**, *401*, 4.
- [51] K. Xu, *Chem. Rev.* **2004**, *104*, 4303.
- [52] C. Janiak, *J. Chem. Soc., Dalton Trans.* **2000**, 3885.
- [53] S. Alvarez, *Dalton Trans.* **2013**, *42*, 8617.
- [54] A. Eisele, K. Kyriakos, R. Bhandary, M. Schönhoff, C. M. Papadakis, B. Rieger, *J. Mater. Chem. A* **2015**, *3*, 2942.
- [55] M. Singh, O. Odusanya, G. M. Wilmes, H. B. Eitouni, E. D. Gomez, A. J. Patel, V. L. Chen, M. J. Park, P. Fragouli, H. Iatrou, N. Hadjichristidis, D. Cookson, N. P. Balsara, *Macromolecules* **2007**, *40*, 4578.
- [56] B. X. Dong, M. Smith, J. Strzalka, H. Li, A. J. McNeil, G. E. Stein, P. F. Green, *J. Polym. Sci., Part B: Polym. Phys.* **2018**, *56*, 652.
- [57] S. Himmelberger, D. T. Duong, J. E. Northrup, J. Rivnay, F. P. V. Koch, B. S. Beckingham, N. Stingelin, R. A. Segalman, S. C. B. Mannsfeld, A. Salleo, *Adv. Funct. Mater.* **2015**, *25*, 2616.
- [58] S. Z. D. Cheng, Y. Yoon, A. Zhang, E. P. Savitski, J.-Y. Park, V. Percec, P. Chu, *Macromol. Rapid Commun.* **1995**, *16*, 533.
- [59] V. M. Kaganer, I. R. Peterson, R. M. Kenn, M. C. Shih, M. Durbin, P. Dutta, *J. Chem. Phys.* **1995**, *102*, 9412.
- [60] V. Marcon, G. Raos, *J. Am. Chem. Soc.* **2006**, *128*, 1408.
- [61] V. Marcon, G. Raos, *J. Phys. Chem. B* **2004**, *108*, 18053.
- [62] S. W. I. Siu, K. Pluhackova, R. A. Böckmann, *J. Chem. Theory Comput.* **2012**, *8*, 1459.

- [63] W. L. Jorgensen, D. S. Maxwell, J. Tirado-Rives, *J. Am. Chem. Soc.* **1996**, *118*, 11225.
- [64] S. Plimpton, *J. Comput. Phys.* **1995**, *117*, 1.
- [65] J. A. Anderson, C. D. Lorenz, A. Travesset, *J. Comput. Phys.* **2008**, *227*, 5342.
- [66] Y. Sun, P. Padmanabhan, M. Misra, F. A. Escobedo, *Soft Matter* **2017**, *13*, 8542.
- [67] A. J. Crane, F. J. Martínez-Veracoechea, F. A. Escobedo, E. A. Müller, *Soft Matter* **2008**, *4*, 1820.
- [68] H. S. Marsh, E. Jankowski, A. Jayaraman, *Macromolecules* **2014**, *47*, 2736.
- [69] H. Lee, A. H. de Vries, S.-J. Marrink, R. W. Pastor, *J. Phys. Chem. B* **2009**, *113*, 13186.
- [70] A. Chaimovich, M. S. Shell, *J. Chem. Phys.* **2011**, *134*, 094112.
- [71] J. J. Uusitalo, H. I. Ingólfsson, P. Akhshi, D. P. Tieleman, S. J. Marrink, *J. Chem. Theory Comput.* **2015**, *11*, 3932.
- [72] M. Campione, S. Tavazzi, M. Moret, W. Porzio, *J. Appl. Phys.* **2007**, *101*, 083512.
- [73] J.-P. Hansen, I. R. McDonald, *Theory of Simple Liquids: With Application to Soft Matter*, Academic, San Diego, CA **2013**.
- [74] J. D. Bjorken, S. J. Brodsky, *Phys. Rev. D* **1970**, *1*, 1416.
- [75] B. K. Money, J. Swenson, *Macromolecules* **2013**, *46*, 6949.
- [76] D. K. Paul, R. McCreery, K. Karan, *J. Electrochem. Soc.* **2014**, *161*, F1395.
- [77] C. G. Arges, Y. Kambe, H. S. Suh, L. E. Ocola, P. F. Nealey, *Chem. Mater.* **2016**, *28*, 1377.
- [78] S. Lascaud, M. Perrier, A. Vallee, S. Besner, J. Prud'homme, M. Armand, *Macromolecules* **1994**, *27*, 7469.
- [79] H. Shimura, M. Yoshio, K. Hoshino, T. Mukai, H. Ohno, T. Kato, *J. Am. Chem. Soc.* **2008**, *130*, 1759.
- [80] M. Yoshio, T. Kagata, K. Hoshino, T. Mukai, H. Ohno, T. Kato, *J. Am. Chem. Soc.* **2006**, *128*, 5570.
- [81] S. Yazaki, Y. Kamikawa, M. Yoshio, A. Hamasaki, T. Mukai, H. Ohno, T. Kato, *Chem. Lett.* **2008**, *37*, 538.
- [82] A. M. van de Craats, N. Stutzmann, O. Bunk, M. M. Nielsen, M. Watson, K. Müllen, H. D. Chanzy, H. Sirringhaus, R. H. Friend, *Adv. Mater.* **2003**, *15*, 495.
- [83] A. M. van de Craats, J. M. Warman, *Adv. Mater.* **2001**, *13*, 130.
- [84] N. Yoshimoto, J. Hanna, *Adv. Mater.* **2002**, *14*, 988.
- [85] M. Funahashi, *Polym. J.* **2009**, *41*, 459.
- [86] M. Funahashi, F. Zhang, N. Tamaoki, *Adv. Mater.* **2007**, *19*, 353.
- [87] F. Zhang, M. Funahashi, N. Tamaoki, *Org. Electron.* **2009**, *10*, 73.
- [88] K. Oikawa, H. Monobe, K. Nakayama, T. Kimoto, K. Tsuchiya, B. Heinrich, D. Guillon, Y. Shimizu, M. Yokoyama, *Adv. Mater.* **2007**, *19*, 1864.
- [89] A. J. J. M. van Breemen, P. T. Herwig, C. H. T. Chlon, J. Sweelssen, H. F. M. Schoo, S. Setayesh, W. M. Hardeman, C. A. Martin, D. M. de Leeuw, J. J. P. Valetton, C. W. M. Bastiaansen, D. J. Broer, A. R. Popa-Merticaru, S. C. J. Meskers, *J. Am. Chem. Soc.* **2006**, *128*, 2336.
- [90] W. Pisula, A. Menon, M. Stepputat, I. Lieberwirth, U. Kolb, A. Tracz, H. Sirringhaus, T. Pakula, K. Müllen, *Adv. Mater.* **2005**, *17*, 684.
- [91] A. E. A. Contoret, S. R. Farrar, P. O. Jackson, S. M. Khan, L. May, M. O'Neill, J. E. Nicholls, S. M. Kelly, G. J. Richards, *Adv. Mater.* **2000**, *12*, 971.
- [92] M. P. Aldred, A. E. A. Contoret, S. R. Farrar, S. M. Kelly, D. Mathieson, M. O'Neill, W. C. Tsoi, P. Vlachos, *Adv. Mater.* **2005**, *17*, 1368.
- [93] S. Yazaki, M. Funahashi, J. Kagimoto, H. Ohno, T. Kato, *J. Am. Chem. Soc.* **2010**, *132*, 7702.
- [94] Z. Jiang, *J. Appl. Crystallogr.* **2015**, *48*, 917.
- [95] B. X. Dong, J. Strzalka, Z. Jiang, H. Li, G. E. Stein, P. F. Green, *ACS Appl. Mater. Interfaces* **2017**, *9*, 44799.